Science and Technology of Advanced Materials

ISSN: 1468-6996 (Print) 1878-5514 (Online) Journal homepage: www.tandfonline.com/journals/tsta20

Berry curvature driven transverse thermoelectric generation in topological magnets

Akito Sakai & Satoru Nakatsuji

To cite this article: Akito Sakai & Satoru Nakatsuji (16 Sep 2025): Berry curvature driven transverse thermoelectric generation in topological magnets, Science and Technology of Advanced Materials, DOI: 10.1080/14686996.2025.2554047

To link to this article: https://doi.org/10.1080/14686996.2025.2554047

Publisher: Taylor & Francis & The Author(s). Published by National Institute for Materials Science in partnership with Taylor & Francis Group.
Journal:*Science and Technologyof Advanced Materials*
DOI:10.1080/14686996.2025.2554047

ARTICLE TYPE: REVIEW

Berry curvature driven transverse thermoelectric generation in topological magnets

Akito Sakai[a] and Satoru Nakatsuji[a-e]

[a]Department of Physics, University of Tokyo, Bunkyo-ku, Tokyo 113-0033, Japan; [b]Institute for Solid State Physics, University of Tokyo, Kashiwa, Chiba 277-8581, Japan; [c]Institute for Quantum Matter and Department of Physics and Astronomy, Johns Hopkins University, Baltimore, Maryland 21218, USA; [d]Trans-scale Quantum Science Institute, University of Tokyo, Bunkyo-ku, Tokyo 113-8654, Japan; [e]Canadian Institute for Advanced Research (CIFAR), Toronto, Ontario M5G 1M1, Canada

ARTICLE HISTORY
Compiled July 30, 2025

ABSTRACT
Topological magnets such as magnetic Weyl and nodal-line semimetals possess topologically non-trivial band structures in magnetically ordered states. In this class of materials, the Berry curvature in momentum space can be significantly enhanced, resulting in thermoelectric responses that exceed empirical scaling laws based on magnetization. Such large transverse thermoelectric effects enable flexible thin-filmbased lateral device structures, leading to novel energy-harvesting technologies and sensors beneficial for Internet of Things (IoT) sensors and wearable devices. In this review, we outline recent progress in the study of the large transverse thermoelectric effects in topological magnets.

KEYWORDS
topological magnets; Weyl semimetals; nodal line semimetals; anomalous Nernst effect

1. Introduction

Thermoelectric effects, such as the Seebeck effect, directly convert heat into electricity (and vice versa) in solids and have been extensively studied for applications in heat exchange, waste heat utilization, and as power sources for IoT sensors [1, 2, 3]. In particular, Peltier devices based on the Seebeck effect are now widely used as wearable coolers (Fig. 1). Recently, the transverse thermoelectric conversion in magnets, known as the anomalous Nernst effect (ANE), has attracted much attention because it allows a lateral configuration of the thermoelectric modules that can efficiently cover heat sources (Fig. 1) [4, 5, 6, 7]. Extensive studies on the transverse thermodynamic effects have identified topological magnets as a key material class exhibiting a large ANE [7], which we review in this article.

Recent developments in condensed matter physics have revealed that non-trivial topological band structures near the Fermi energy ε_F are important for understanding the unique properties of materials [8, 9, 10, 11]. Among them, topological magnets

Email: akito@phys.s.u-tokyo.ac.jp, satoru@phys.s.u-tokyo.ac.jp

such as magnetic Weyl semimetals and nodal-line semimetals have been found to exhibit large transverse responses such as the ANE and anomalous Hall effect (AHE) [12, 13, 14, 15, 16, 17, 18, 19, 20, 21, 22, 23, 24, 25, 26, 27, 5, 7, 28] owing to the non-vanishing momentum-space (k-space) Berry curvature. Various research groups have demonstrated ANE-based thermoelectric devices [4, 29, 30, 31, 32, 33, 34, 35], which may be useful for energy harvesting from waste heat, IoT sensors, and wearable devices.

In this article, we review the recent advances in research and development of transverse thermoelectric generation in topological magnets. We first introduce the ANE as the transverse thermoelectric generation for magnetic materials (Sec. 2). Then, we briefly illustrate the theoretical framework for the Berry curvature–driven intrinsic ANE in topological magnets (Secs. 3-5). We also review the experimental observations for ANE in various typical topological magnets (Sec. 6). Finally, we provide a summary and perspective (Sec. 7).

2. Anomalous Nernst effect –transverse thermoelectric effect in magnetic mateirals

Generally in solids, the electric current density $\mathbf{J}_c$, is proportional to the electric field $\mathbf{E}$, $\mathbf{J}_c = \sigma\mathbf{E}$, known as Ohm's law. Similarly, the heat current density $\mathbf{J}_q$ is proportional to the temperature gradient ∇T, $\mathbf{J}_q = \kappa(-\nabla T)$, known as Fourier's law. Here, σ and κ are electric and thermal conductivity tensors. In metals and semiconductors, carriers (electrons or holes) transport both electric and heat current. This means that $\mathbf{E}$ (∇T) also generates $\mathbf{J}_q$ ($\mathbf{J}_c$). Thus, the above equations are generalized in the linear response regime as,

$$\mathbf{J}_c = \sigma\mathbf{E} + \alpha(-\nabla T), \quad (1)$$

$$\mathbf{J}_q = \Pi\mathbf{E} + \kappa(-\nabla T). \quad (2)$$

The newly added cross-correlated terms represent the thermoelectric effects with thermoelectric tensors α and Π. According to the Onsager reciprocal relations, α and Π are not independent and satisfy $\Pi = \alpha T$ [36, 37, 38]. Besides, the Onsager reciprocal relations also hold for the off-diagonal terms of the conductivity tensors,

$$\sigma_{ij}(B) = \sigma_{ji}(-B), \alpha_{ij}(B) = \alpha_{ji}(-B), \kappa_{ij}(B) = \kappa_{ji}(-B), \quad (3)$$

where σ_{ji}, α_{ji} and κ_{ji} are respectively called Hall conductivity, transverse thermoelectric conductivity and thermal Hall conductivity, and B is the magnetic field. The Eq. (3) implies $\sigma_{ji} = \alpha_{ji} = \kappa_{ji} = 0$ when both magnetic field B and magnetization M are zero ($B = M = 0$).

The Onsager reciprocal relations are fundamental for irreversible transport processes originating from microscopic time-reversal symmetry. Thus, they are never

violated as long as the system satisfies their precondition; the states at $+B$ and $-B$ are equivalent to each other after the time-reversal operation. In other words, the relations such as $\sigma_{ij}(B) \neq \sigma_{ji}(-B)$, $\alpha_{ij}(B) \neq \alpha_{ji}(-B)$, may occur in hysteretic regimes due to magnetic domains or exchange bias. Additionally, *non*-Onsager quantities such as the Nernst coefficient S_{ij} (defined as Eq. (8) below) do not obey this rule. Thus, $S_{ij}(B)$ is not necessarily equal to $S_{ji}(-B)$ as observed in $YbMnBi_2$ [25, 26]. (These two cases should not be called "violations" of the Onsager relations since they simply fall outside the scope of the principles.)

Anomalous Hall effect

The electrical resistivity ρ is the inverse of σ, $\rho = \sigma^{-1}$, and xx and xy components are given by

$$\sigma_{xx} = \frac{\rho_{yy}}{\rho_{xx}\rho_{yy} - \rho_{xy}\rho_{yx}}, \ \sigma_{xy} = -\frac{\rho_{xy}}{\rho_{xx}\rho_{yy} - \rho_{xy}\rho_{yx}}, \tag{4}$$

where we consider the net flow of carriers along the xy plane, $\mathbf{J}_c \perp \mathbf{z} \parallel \mathbf{B}$. Thus, we get $\sigma_{xx} \sim 1/\rho_{xx}$, $\sigma_{yx} = -\sigma_{xy} \sim -\rho_{yx}/\rho^2_{xx}$ for conventional isotropic 3D metals where $\rho_{xx} \sim \rho_{yy} \gg |\rho_{yx}|$ and $\rho_{xy}(B) = -\rho_{yx}(B)$. Experimentally, we measure $\rho_{xx} = J_x/E_x$, and $\rho_{yx} = E_y/J_x$ and obtain σ_{xx} and σ_{xy}, where J_i and E_i are the applied current density and measured electric field along i-direction, respectively.

Historically, Edwin Hall first discovered the Hall effect in nonmagnetic metals and ferromagnets [39, 40]. Subsequent studies have established the empirical relation

$$\rho_{yx} = R_0 B + R_s M, \tag{5}$$

where R_0 and R_s are the ordinary Hall and anomalous Hall coefficients, respectively [41]. The first term is the ordinary Hall effect (OHE), related to the carrier density n and charge q as $R_0 = B/(nq)$. The second term represents the anomalous Hall effect (AHE), which typically dominates in ferromagnetic states. This has been intuitively interpreted as the consequence of the Lorentz force due to M, and thus it was long believed that AHE should not occur in antiferromagnets, where M is vanishingly small.

However, this empirical relation (Eq. (5)) and the corresponding intuitive interpretation have turned out to be inaccurate; they neglect contributions from Berry curvatures in both real and momentum space. The real-space Berry curvature originates, for example, from skyrmions in noncentrosymmetric magnets [42, 43, 44, 45, 46, 47, 48]. The k-space Berry curvature leads to the intrinsic AHE, which is distinct from the extrinsic AHE caused by disorder-related mechanisms such as skew scattering and side jump. Importantly, the intrinsic AHE is not necessarily proportional to M and can be significant in noncollinear and noncoplanar antiferromagnets (AFM) [49, 50, 51, 7, 28] and even finite in the collinear antiferromagnetic known as altermagnets [52, 53, 54, 55]. In Sec. 4, we discuss the intrinsic (k-space Berry curvature driven) AHE in detail and explain how large AHE signals can arise in both ferromagnets and antiferromagnets.

Anomalous Nernst effect

The longitudinal thermoelectric effect, the Seebeck coefficient S_{ii}, is obtained by setting $\mathbf{J}_c = 0, \nabla T \parallel \mathbf{x}$ and $\sigma_{ij} = \alpha_{ij} = 0$ in Eq. (1),

$$S_{xx} \equiv \frac{E_x}{-(\partial T/\partial x)} = \frac{V}{\Delta T} = \frac{\alpha_{xx}}{\sigma_{xx}}. \tag{6}$$

Note that the sample length cancels out and does not appear in Eq. (6) (see Fig. 2 (a)).

In contrast, the transverse thermoelectric effect (Nernst effect) can be finite by breaking the time-reversal symmetry i.e., $B \neq 0$ or $M \neq 0$. Similar to the Hall effect, B-linear and M-linear terms are called ordinary Nernst effect (ONE) and ANE, respectively.

By setting $\mathbf{J}_c = 0, \nabla T \parallel \mathbf{x}$ in Eq. (1), we get

$$\alpha_{yx} = \sigma_{yx} S_{xx} + \sigma_{yy} S_{yx}, \tag{7}$$

where the Nernst coefficient S_{yx} is defined as

$$S_{yx} \equiv \frac{E_y}{-(\partial T/\partial x)} = \frac{\ell_T}{\ell_V} \frac{V_y}{\Delta T}. \tag{8}$$

Interestingly, the Nernst voltage V_y is proportional not only to the temperature difference ΔT but also to the sample geometry ℓ_V/ℓ_T, where ℓ_V and ℓ_T respectively represent distances between voltage and temperature terminals (Fig. 2 (b)). Thus, one can enhance V_y in thin-film thermopile structure by reducing ℓ_T and increasing ℓ_V (Fig. 1 (b)), as demonstrated by various experiments [5, 4, 30, 31, 32, 56, 34]. Eq. (7) immediately provides

$$-S_{yx} = -\alpha_{yx}\rho_{yy} + \sigma_{yx}\rho_{yy} S_{xx} \equiv S_1 + S_2. \tag{9}$$

Here, S_1 and S_2 respectively indicate the contributions directly from α_{yx} and longitudinal thermoelectric effect S_{xx} converted to the transverse direction through σ_{xy}. Thus, in addition to large $|\alpha_{yx}|$, these two contributions should be constructive (namely sgn $(-\alpha_{yx})$ = sgn $(\sigma_{yx} S_{xx})$) for enhancing $|S_{yx}|$.

3. Berry phase, Berry connection and Berry curvature

Topology in condensed matter physics appears from the Hilbert space geometry [57]. For simplicity, let us assume a nondegenerate complete orthonormal system $\{|u_n\rangle\}$

$$\mathrm{H}(\mathbf{R})|u_n(\mathbf{R})\rangle = E_n(\mathbf{R})|u_n(\mathbf{R})\rangle, \tag{10}$$

where E_n is the eigenenergy for the n-th eigen state $|u_n\rangle$, and $\mathbf{R}(\mathbf{t})$ is a parameter for the Hamiltonian $\mathrm{H}(\mathbf{R})$ such as the wave vector $\mathbf{k}$ and real space position $\mathbf{r}$. Then, the time-

evolution for the initial state $|\psi(t)\rangle = \sum_n c_n |u_n(\mathbf{R})\rangle$ obtained from the timedependent schr¨odinger equation $i\hbar\frac{d}{dt}|\psi(t)\rangle = \mathcal{H}(\mathbf{R})|\psi(t)\rangle$ is

$$i\hbar\frac{d}{dt}c_n + i\hbar c_n \langle u_n|\frac{d}{dt}|u_n\rangle + i\hbar\sum_{m\neq n}\frac{\langle u_n|\frac{d}{dt}\mathcal{H}|u_m\rangle}{E_m - E_n}c_m = c_n E_n \quad . \tag{11}$$

On the other hand, the time derivative of Eq. (10) gives $\langle u_n|\frac{d}{dt}|u_m\rangle = \frac{\langle u_n|\frac{d}{dt}\mathcal{H}|u_m\rangle}{E_m - E_n}$ for $n \neq m$. This indicates the last term on the left-hand side of Eq. (11) is negligible compared to the diagonal term $\langle u_n|\frac{d}{dt}|u_n\rangle$ in the adiabatic approximation, where the time-evolved state stays at the initial eigenstate with a certain phase difference ϕ; $|u_n(\mathbf{R}(t))\rangle \sim |u_n(\mathbf{R}(0))\rangle\exp(i\phi)$. Solving Eq. (11), we obtain

$$c_n(t) = c_n(0)\exp(i\theta_n(\mathbf{R}))\exp(i\gamma_n(\mathbf{R})), \tag{12}$$

where $\theta_n(\mathbf{R}) \equiv -\frac{1}{\hbar}\int_{\mathbf{R}_0}^{\mathbf{R}} E_n(\mathbf{R}')d\mathbf{R}'$ and $\gamma_n(\mathbf{R}) \equiv i\int_{\mathbf{R}_0}^{\mathbf{R}} \langle u_n(\mathbf{R}')|\frac{\partial}{\partial\mathbf{R}'}|u_n(\mathbf{R}')\rangle\, d\mathbf{R}'$ are known as the dynamical and geometrical phases, respectively. The former is the conventional term originating from the time evolution of the eigenstate. The latter is the topological term depending on the path C from $\mathbf{R}_0$ to $\mathbf{R}$. While the above $\gamma_n(\mathbf{R})$ is gauge-*dependent* and not a physical observable, the closed-loop integral so-called the Berry phase

$$\gamma_n \equiv \oint_C \mathbf{A}_n(\mathbf{R}')d\mathbf{R}' = \int_S \mathbf{\Omega}_n(\mathbf{R}')d\mathbf{S}' \quad \gamma(C) \tag{13}$$

becomes gauge-*independent*. Here,

$$\mathbf{A}_n(\mathbf{R}) \equiv i\langle u_n(\mathbf{R})|\nabla_{\mathbf{R}}|u_n(\mathbf{R})\rangle \tag{14}$$

and

$$\mathbf{\Omega}_n(\mathbf{R}') \equiv \nabla_{\mathbf{R}} \times A_n(\mathbf{R}) \tag{15}$$

are the Berry connection and Berry curvature, respectively. In real space, $\gamma_n(C)$,$\mathbf{A}_n(\mathbf{r})$,$\mathbf{\Omega}_n(\mathbf{r})$ correspond to the Aharonov–Bohm phase, vector potential and magnetic field, respectively. In this review, we focus on the k-space Berry curvature $\mathbf{\Omega}_n(\mathbf{k}) = \nabla_{\mathbf{k}} \times \mathbf{A}_n(\mathbf{k}) = i\nabla_{\mathbf{k}} \times \langle u_n(\mathbf{k})|\nabla_{\mathbf{k}}|u_n(\mathbf{k})\rangle$ as an origin of the large transverse responses in topological magnets, where $|u_n(\mathbf{k})\rangle$ is the periodic part of the Bloch wave function $|\psi_{n,\mathbf{k}}\rangle = e^{i\mathbf{kr}}|u_n(\mathbf{k})\rangle$.

4. Berry curvature driven intrinsic transverse thermoelectric effect

Similar to σ_{ij}, α_{ij} can originate from both intrinsic and extrinsic mechanisms. Here, the term "intrinsic" refers to the contribution from the k-space Berry curvature as discussed in Sec. 2. In MnBi, the experimentally observed α_{ij} is one order of magnitude larger than the theoretical value assuming the intrinsic mechanism, indicating large

extrinsic contributions [58]. However, this is so far an exception; the intrinsic mechanism dominates in most of magnetic materials with large ANE. Thus, in this review, we focus on the intrinsic ANE driven by *k*-space Berry curvature. In this section, we first introduce the mechanism for the intrinsic AHE as it is related to the origin of the intrinsic ANE.

Intrinsic Anomalous Hall conductivity

Using Kubo-formula we obtain [59, 60]

$$\sigma_{xy}(T,\mu) = -\frac{e^2}{\hbar}\int \frac{d^D k}{(2\pi)^D}\sum_n f_{n\mathbf{k}}\Omega_n^z(\mathbf{k}), \tag{16}$$

where D(= 2,3), e, ℏ, μ, $\varepsilon_{n\mathbf{k}}$, and $f_{n\mathbf{k}} = 1/(e^{(\varepsilon_{n\mathbf{k}}-\mu)/k_BT}+1)$ are the spatial dimension of the system, elementary charge, reduced Planck constant, chemical potential, energy for the band n, and the Fermi-Dirac distribution function, respectively. The equation (16) yields the quantum Hall effect for 2D-band insulator at $T = 0$

$$\sigma_{xy}^{\mathrm{QHE}} = -\frac{e^2}{\hbar}\int_{BZ}\frac{d^2k}{(2\pi)^2}\sum_{n}^{\text{occupied}}\Omega_n^z(\mathbf{k}) = -\frac{e^2}{\hbar}C, \tag{17}$$

where C = 1,2,3⋯ is the Chern number and matches with the number of occupied states [61]. Thus, the intrinsic AHE in 3D metals can be viewed as an "unquantized" version of the quantum Hall effect. The Berry curvature $\Omega^z_n(\mathbf{k})$ in Eq. (16) is numerically computed by using

$$\Omega_n^z(\mathbf{k}) = -2\mathrm{Im}\sum_{m\neq n}\frac{\langle u_n(\mathbf{k})|\frac{\partial H(\mathbf{k})}{\partial k_x}|u_m(\mathbf{k})\rangle\langle u_m(\mathbf{k})|\frac{\partial H(\mathbf{k})}{\partial k_y}|u_n(\mathbf{k})\rangle}{(\varepsilon_{m\mathbf{k}}-\varepsilon_{n\mathbf{k}})^2}, \tag{18}$$

which means that the magnitude of the Berry curvature $|\Omega_n^z(\mathbf{k})|$ becomes singularly large when two bands touch. This explains why topological magnets with band crossings (Fig. 4 and Sec. 5) show a large AHE.

In ferromagnets, the spontaneous time-reversal symmetry breaking ensures a finite σ_{xy}. By contrast, antiferromagnets require additional constraints for the non-vanishing AHE, i.e. $\sigma_{xy} = 0$ for the simplest collinear anitiferromagnets, where the spin structure is invariant time-reversal + half-unit cell translation [62, 63, 28]. Examples include Mn_3X (X = Sn, Ge) as shown in Sec 6.

Intrinsic transverse thermoelectric conductivity

Similar to σ_{xy}, the transverse thermoelectric conductivity α_{xy} also arises from the intrinsic Berry curvature mechanism [64], i.e.,

$$\alpha_{xy}(T,\mu) = \frac{|e|}{T\hbar}\int \frac{d\mathbf{k}}{(2\pi)^3}\Omega_{n,z}(\mathbf{k})\{(\varepsilon_{n\mathbf{k}}-\mu)f_{n\mathbf{k}} + k_{\mathrm{B}}T\log[1+e^{-\beta(\varepsilon_{n\mathbf{k}}-\mu)}]\} \quad (19)$$

$$= \frac{1}{|e|}\int d\varepsilon\ \sigma_{xy}(0,\varepsilon)\frac{\varepsilon-\mu}{T}\left(-\frac{\partial f}{\partial \varepsilon}\right) \quad (20)$$

$$= -\frac{k_{\mathrm{B}}}{|e|}\int d\varepsilon \frac{\partial \sigma_{xy}(T,\varepsilon)}{\partial \varepsilon} s(\varepsilon,T), \quad (21)$$

where $s = -f\ln(f) - (1-f)\ln(1-f)$ is the entropy density and $\partial\sigma_{xy}/\partial\varepsilon = \sum_{n\mathbf{k}} \Omega_{n,z}(\mathbf{k})\delta(\varepsilon-\varepsilon_{n\mathbf{k}})$. Using the Sommerfeld expansion we obtain the low-temperature asymptotic form called the Mott relation

$$\alpha_{xy} = -\frac{\pi^2 k_{\mathrm{B}}^2 T}{3|e|}\frac{\partial \sigma_{xy}(0,\ \varepsilon)}{\partial \varepsilon}\bigg|_{\varepsilon=E_F}. \quad (22)$$

This implies that α_{xy}/T becomes large when σ_{xy} varies rapidly as a function of ε owing to topological band structures (Fig. 3) [65].

σ_{xy} and α_{xy} are often numerically computed using Eq. (16) and Eq. (19) by firstprinciples calculations, respectively. While σ_{xy} is given by the sum of the Berry curvature below $\epsilon \sim \mu$ (Eq. (16)), α_{xy} depends on the Berry curvature and density of states (DOS) near $\epsilon \sim \mu$ (Eq. (19)). Thus, topological flat band structures that produce both large Berry curvature and DOS near the Fermi energy are essential for enhancing α_{xy}. Examples include the titled Weyl cones (Co_2MnGa) [18], nodal web structure (Fe_3Ga) [21, 66], and nodal plane (Fe_3Sn) [24], as discussed in Sec. 5.

5. Topological band structures inducing large Berry curvatures

As discussed in Sec. 4, Berry curvature is highly enhanced near band crossings. Such band crossings occur at either (i) a k point (Weyl point, Fig. 4(a)), (ii) a line (nodal line, Fig. 4(b)), or (iii) a plane (nodal plane, Fig. 4(c)). The nodal line and plane are defined in the absence of the spin-orbit coupling (SOC). After introducing SOC, Weyl points may persist, otherwise a small gap opens all over the nodal line (plane).

The Weyl point denotes a non-degenerate linear band crossing $\varepsilon_{\mathbf{k}} \sim \pm v|\mathbf{k}\pm\mathbf{k}_0|$ and their model Hamiltonian is identical to the time-independent Weyl equation $H\psi_{\mathbf{k}} \sim \pm v(\mathbf{k}\pm\mathbf{k}_0)\sigma\psi_{\mathbf{k}} = \varepsilon_{\mathbf{k}}\psi_{\mathbf{k}}$ [12, 13, 67]. In particular, non-vanishing AHE and ANE appear in magnetic Weyl semimetals (i.e. Weyl magnets), possessing Weyl points near the Fermi energy ε_F in a magnetically ordered state. Each Weyl point carries the chirality of ±1 and always pairs with the opposite signs [68]. These Weyl points act as either sources or sinks of the Berry curvature (Fig. 4(a)), inducing AHE and ANE.

6. Experimental realization –large ANE in topological magnets

Until now, various topological magnets have been discovered that exhibit large ANEs. In this section, we first describe the universal features shared across these materials, followed by details on specific compounds. The materials highlighted here are some of

the the best-studied topological magnets, i.e., Mn_3X (X = Sn, Ge) [15, 16, 17, 22], Co_2MnGa [18], Fe_3X (X = Ga, Al) [21], $YbMnBi_2$ [25, 26], Fe_3Sn [24], $Co_3Sn_2S_2$ [19, 20] and $UCo_{0.8}Ru_{0.2}Al$ [23].

(1) Dominant intrinsic contribution to σ_{xy} and α_{xy}.

The intrinsic Berry curvature contribution dominates both σ_{xy} and α_{xy} in topological magnets. For example, first-principles calculation that consider only the intrinsic contribution (Eq. (16) and Eq. (19)) successfully reproduce the experimental σ_{xy} and α_{xy}. The enhanced σ_{xy} and α_{xy} are associated with topological band structures, which are often confirmed by the ARPES (Angle-resolved Photoemission Spectroscopy) measurements. In most of these topological magnets, electron correlation effects are included only through the bandwidth renormalization, characterized by the ratio of Sommerfeld coefficient between experiment and theory, $\gamma_{\mathrm{exp}}/\gamma_{\mathrm{theory}}$.

Another piece of evidence supporting the intrinsic contribution is the scaling relation between the anomalous Hall conductivity σ_{xy} and longitudinal conductivity σ_{xx} [69]. According to the scaling relation , σ_{xy} is almost constant and reaches $\sim e^2/(ha) \sim 10^3\ \Omega^{-1}\mathrm{cm}^{-1}$ in the good metal regime $\sigma_{xx} \sim 3\times10^3\ \Omega^{-1}\mathrm{cm}^{-1}$ - $5\times10^5\ \Omega^{-1}\mathrm{cm}^{-1}$ [69]. As shown in Figs. 5 (a) and (b), the topological magnets exhibit $|\sigma_{ij}| \sim e^2/(ha)$ and satisfy these conditions.

(2) Relation between ANE and magnetization.

As mentioned above, the intrinsic σ_{xy} and α_{xy} originate from the k-space Berry curvature and thus they do not necessarily scale with the saturation magnetization. However, this is typically observed only at low T(where M is nearly saturated) and at high B (single-domain state). In other words, at high T and low B, ANE and AHE are usually related to the magnetization.

(i) Temperature dependence (Fig. 7 (a))

The AHE and ANE vanish above Curier temperature T_C (or N´eel temperature T_N) since they require spin-split band structure due to the time-reversal symmetry breaking. For instance, in Weyl magnets, Weyl points with opposite chirality annihilate into a four-fold degenerate Dirac point above $T_{C,N}$. On cooling below $T_{C,N}$, local magnetic moments $\langle m\rangle$ develop and induce spin splitting in the band structure. The size of $\langle m\rangle$ ($\langle m\rangle \propto M$ for ferromagnets) is usually a good indicator for the magnitude of spin-splitting (and distance between Weyl points for Weyl magnets). Thus T dependence of ANE and AHE resembles that for M near $T_{C,N}$. In particular, this is evident for low $T_{C,N}$ materials such as $YbMnBi_2$, $Co_3Sn_2S_2$, and $UCo_{0.8}Ru_{0.2}Al$ (Fig. 11(b)) [25, 26, 20, 23]. Since the first-principles calculations normally fix the moment size $\langle m\rangle$, a comparison to the experiment should be performed at $T \ll T_C$, where the magnetization becomes nearly T independent.

(ii) Magnetic field dependence (Fig. 7 (b))

At high B, the Berry curvature Ω_z dominates σ_{xy} and α_{xy}, leading to the violation of the empirical scaling relation with the saturation magnetization M_s. On the other hand, at low B, the curves of $S_{xy}(B)$ and $\rho_{xy}(B)$ resemble that of $M(B)$, as magnetic domains are not fully aligned. Namely, integrating the contributions from all the magnetic domains

that have either parallel or antiparallel M to the magnetic field direction, S_{xy} and ρ_{xy} are generally proportional to M since the sign of each domain's contribution depends on its magnetization direction (Fig. 7 (b)).

The zero-field spontaneous ANE is important for thermoelectric applications. This occurs in hard magnets with large magnetocrystalline anisotropy K_u [J/m^3] and small saturation magnetization M_s [A/m], i.e., larger magnetic hardness parameter κ_h than unit; $\kappa_h = \sqrt{\frac{K_u}{\mu_0 M_s^2}} > 1$ [70]. For soft magnets such as Co_2MnGa, Fe_3X (X = Ga, Al) and Fe_3Sn shown below, zero-field spontaneous ANE occurs only in thin-film form under perpendicular temperature gradient to the film plane since the shape anisotropy stabiles the in-plane magnetization.

(3) Diverging behavior of α_{xy}/T (Fig. 8)

At low T, α_{xy}/T should be constant as expected from the Mott relation (Eq. (22)), and finally $\alpha_{xy} = 0$ at $T = 0$. On the other hand, various topological magnets show $\alpha_{xy}/T \sim -\ln T$ at high T (Fig. 8 (a)). This logarithmic enhancement arises from the anomalous enhancement of $\sigma_{xy}(\epsilon)$ and $\alpha_{xy}(\epsilon)$ due to the topological flat band structure (Sec 4 & Fig. 3), which is also reproduced by the first-principles calculations for Co_2MnGa and Fe_3Ga (Fig. 8 (b)) [18, 21, 66]. As the topological flat band approaches the Fermi energy E_F, α_{xy} shows $-\ln T$ divergence to lower temperatures (Fig. 8 (b)).

Mn_3X (X = Sn, Ge)

The realization of the spontaneous AHE without net magnetization has been a great challenge in condensed matter physics. It was first discovered in the chiral spin liquid state of $Pr_2Ir_2O_7$ at low temperatures [51] and later found in the inverse-triangular spin state of Mn_3Sn at room temperature [15]. Mn_3X (X = Sn, Ge) has a hexagonal Ni_3Sn-type ($D0_{19}$) crystal structure (space group $P6_3/mmc$), where Mn atoms form breathing-type kagome layers in the ab plane [71]. Mn_3X exhibits inverse-triangular non-collinear antiferromagnetic ordering at $T_N \sim 430$ K (X = Sn) and 372 K (X = Ge) (Table 1) with a vanishingly small net spontaneous magnetization of several mμ_B in ab plane [72, 73, 74, 75]. Nevertheless, Mn_3X shows a large spontaneous Hall effect [15, 76, 77], Nernst effect [16, 17, 22] and magneto-optical Kerr effect [78, 22, 79] comparable to those for ferromagnets. Besides, Mn_3X also exhibits spintronic phenomena such as the magnetic spin Hall effect [80], electric switching of AFM domains [81, 82, 83] and tunneling magnetoresistance [84]. These interesting properties are intimately linked to the magnetic structure and k-space topology: (1) The magnetic point group symmetry $m'm'm$ for Mn_3Sn is compatible with ferromagnetism, which allows the finite spontaneous AHE and ANE. This situation can be naturally interpreted by considering the magnetic structure as a cluster multipole [63, 85]. (2) The ARPES measurements on Mn_3Sn reveal Weyl points around K point near E_F, consistent with the first-principles calculations [86]. These Weyl points act as sources or sinks of the Berry curvature, enhancing the AHE and ANE.

Mn_3X has been intensively studied for developing antiferromagnetic spintronics devices such as low-power and ultrafast nonvolatile memory [87, 88, 89]. For thermoelectric applications, the absence of stray fields and shape anisotropy in randomly-oriented polycrystalline films has proven better for designing a highly dense

array of the spintronic thermopiles with high heat flux sensitivity, compared to the conventional sensors based on ferromagnets [31].

Co_2MnGa, $Co_2MnAl_{1-x}Si_x$

The above-mentioned ANE for Mn_3Sn is surprisingly large for AFM and comparable to that in ferromagnets. However, its magnitude is still small $|S_{xy}|$ ~0.5 μV/K at room T. A much large ANE $|S_{xy}|$ ~ 6-8 μV/K, over an order of magnitude larger than in conventional magnets, was first reported in the Weyl ferromagnet Co_2MnGa [18, 90, 91, 92]. This remains the largest room-T value reported to date (Fig. 6(a)). The crystal structure of Co_2MnGa is the $L2_1$ ordered cubic full Heusler (space group $Fm\bar{3}m$) and the Curie temperature is T_C ~ 694 K (Table 1) [93]. The Hall conductivity σ_{xy} gradually increases on cooling and reaches σ_{xy} ~ 2000 $\Omega^{-1}cm^{-1}$ (Fig. 6(b)), consistent with the first-principles calcinations. The transverse thermoelectric conductivity α_{xy} for Co_2MnGa first increases on cooling, peaks at ~ 150 K, and finally vanishes at low T (Fig. 6(c)), again consistent with the first-principles calculations after considering the renormalization factor due to the correlation effect. The first-principles calculations attribute the large transverse responses to the enhanced Berry curvature near the tilted Weyl cones (Fig. 9), which ARPES measurements confirm later [94, 95, 96, 97]. The tilted Weyl cone in Co_2MnGa is interpreted as a Lifshitz transition between type-I and type-II Weyl semi-metallic states, where one of the bands becomes nearly flat at $E \sim E_F$. This topological flat band is the key for the large α_{xy} in Co_2MnGa. The large transverse responses for Co_2MnGa are also promising for thermoelectric and spintronics device applications [98, 99, 32].

To date, most thermoelectric applications of the ANE focus on heat flux sensors utilizing the large voltage in the thin-film thermopile structure. Since ANE materials are typically metallic with relatively high thermal conductivity, they are suitable for efficient heat flux sensing. However, power generation from waste heat remains a signif-√ icant challenge. A problem is the low conversion efficiency $\eta_{ANE} = \eta_C \frac{\sqrt{1-Z_{yx}T_{av}}-1}{\sqrt{1-Z_{yx}T_{av}}+1}$ due to the small figure of merit $Z_{yx}T = \sigma_{xx}S_{yx}^2 T/\kappa_{yy}$. For example, even for Co_2MnGa, the ANE material with the largest S_{yx} at room T, $Z_{yx}T$ ~ 0.0001 [18] partly due to the high thermal conductivity. Here, $T_{av} = (T_h + T_c)/2$ and $\eta_C = (T_h - T_c)/T_h$ are the average T between high T_h and low T_c temperatures, and Carnot efficiency, respectively [100]. We note that $\eta_{ANE} \to \eta_C$ at $Z_{yx}T \to 1$, which is different from the Seebeck effect case, where $\eta_{SE} = \eta_C \frac{\sqrt{1+ZT_{av}}-1}{\sqrt{1+ZT_{av}}+T_c/T_h} \to \eta_C$ at $ZT = \sigma_{xx}S_{xx}^2 T/\kappa_{xx} \to \infty$.

When considering applications, material cost is also an important factor. In the case of Co_2MnGa, Ga is rather expensive compared to Co and Mn. Although the ANE S_{xy} ~ 1 μV/K for pure Co_2MnAl is not so large as 6 ~ 8 μV/K in Co_2MnGa, the Si-doping enhances the ANE upto S_{xy} ~ 5.7 μV/K in $Co_2MnAl_{0.63}Si_{0.37}$ [101]. Since both Al and Si are low-cost and naturally abundant elements, the system is promising for industrial applications.

Fe_3X (X=Ga, Al)

The discovery of the large ANE in Co_2MnGa has stimulated the study of thermoelectric applications based on ANE. In addition to the large ANE, low material cost is an important factor for such applications. Iron is abundant and inexpensive, but the ANE for body-centered cubic (bcc) iron (α-Fe) is very small ($|S_{xy}| \sim 0.3\ \mu$V/K). With the help of high-throughput first-principles calculations, a large ANE has been identified in Fe_3X (X = Ga, Al) [21]. Fe_3X (X = Ga, Al) crystallizes in a bcc $D0_3$ structure and shows ferromagnetic order below $T_C \sim$ 720 K (Fe_3Ga) and $\sim$ 600 K (Fe_3Al) [102, 103]. As shown in Fig. 6(a), Fe_3X exhibits a large ANE $-S_{yx} \sim 5.7\ \mu$V/K (Fe_3Ga) and $\sim 4.0\ \mu$V/K (Fe_3Al) at room temperature [21], which is more than an order of magnitude larger than that for bcc iron [104]. The large spontaneous ANE is also confirmed in epitaxial thin films (Fig. 10 (a)). Besides, the room-T α_{xy} is also very large $\alpha_{xy} \sim 5$ ($Am^{-1}K^{-1}$). The first-principles calculations reveal that a nodal web structure –multiple interconnected nodal lines– near the L point gives rise to large Berry curvatures (Fig. 10(b) and (c)) [21, 66]. The large ANE in Fe_3X is robust against chemical doing as found in Fe_xGa_{4-x} ($3.07 < x < 3.12$) and $Fe_3Ga_{1-x}Al_x$ ($0 \leq x \leq 0.6$) polycrystals [105, 106], as well as in epitaxial Fe-Ga thin films without post-annealing [107], which are all found beneficial for thermoelectric applications. For example, flexible heat flux sensors have been fabricated with mass-producible rollto-roll sputtering method (Fig. 10(d) and (e)) [34]. Ribbon-shaped Fe_3Al alloys have also been produced, which can be directly wrapped around heat pipes (Fig. 10(f)) [35]. Fe_3X is also promising for spintronics device applications due to the low Gilbert damping constant [108, 109].

$YbMnBi_2$

Topological antiferromagnets are attractive even for thermoelectric applications in electronic devices owing to their large responses and small stray field. The noncollinear antiferromagnet $YbMnBi_2$ provides a large ANE $-S_{zy} \sim 10\ \mu$V/K at $T \sim 200$ K (Fig. 6(a)) [25, 26]. $YbMnBi_2$ has a primitive tetragonal lattice (nonsymmorphic space group $P4/nmm$) and shows nearly collinear (C-type) AFM along c axis with a small cant along ab-palne below $T_N \sim$ 280 K [110, 111, 112, 25, 26]. The electronic band structure for $YbMnBi_2$ is highly anisotropic, resulting in highly anisotropic transport properties such as $\rho_{zz} > \rho_{yy}$, $S_{yy} < 0 < S_{zz}$ and $S_{yx} = -S_{zx}$. On the other hand, samples are highly sensitive to oxygen and easily change their properties in the air [26]. For instance, the violation of the Onsager relation for σ_{ji} reported in [25] may be caused by the sample degradation [26]. Thus, industrial applications using this material are currently not straightforward.

Fe_3Sn

As discussed in Sec. 4, topological flat bands are key for enhancing the transverse thermoelectric coefficient. Kagome metals are good candidates since s-electrons on the kagome lattice are known to provide a flat band owing to the destructive interference [113, 114]. The kagome ferromagnet Fe_3Sn shares the same crystal structure as Mn_3X (X = Sn, Ge), hexagonal Ni_3Sn type ($D0_{19}$, space group $P6_3/mmc$), where Fe atoms form

a kagome lattice in *ab* plane (Table 1) [115]. The Curie temperature for Fe_3Sn is $T_C \sim$ 760 K, which is high among topological magnets (Table 1). The large ANE $S_{ij} \sim 3\ \mu$V/K at room T in Fe_3Sn was first reported in bulk polycrystals [24] and later in amorphous and epitaxial thin films [116, 117]. As shown in Fig. 6(a), S_{ij} for polycrystalline Fe_3Sn increases linearly at 100 K $\leq T \leq$ 400 K. The first-principles calculations reveal that the large ANE for Fe_3Sn originates from a sharp peak in σ_{yz} at $E - E_F \sim 50$ meV, which comes from a nodal plane –nearly degenerate, partiallyflat bands– near the Brillouin zone boundary [24]. These partially flat bands might originate from the destructive interference in the kagome lattice. The topological ANE found in the thin film based on the amorphous form of Fe_3Sn makes this material attractive for the thermoelectric applications.

$Co_3Sn_2S_2$

A Co-based shandite $Co_3Sn_2S_2$ is another kagome ferromagnet with $T_C \sim 177$ K. It crystallizes in a rhombohedral structure (space group $R\bar{3}m$). The magnetic Weyl semimetal phase in $Co_3Sn_2S_2$ is confirmed by various techniques, including ARPES (Fermi-arcs and linear bulk band crossings), STM (Scanning Tunneling Microscope) (quasi-particle interference), and magnetoresistance (chiral anomaly) [118, 19]. Owing to the strong magnetocrystalline anisotropy and relatively small saturation magnetization $M_s \sim 0.8\ \mu_B$/f.u., the ANE shows clear hysteresis with the sizeable spontaneous value $S_{xy} \sim 3\ \mu$V/K even in bulk form when B is applied along the easy axis $B \parallel c$ (Fig. 11) [20]. While the Curie temperature is lower than room T, these properties are attractive for thermoelectric applications at low T.

$UCo_{0.8}Ru_{0.2}Al$

Another approach for enhancing the DOS at the Fermi energy is via strong electronic correlations, especially in *f*-electron systems. The U-based ferromagnet $UCo_{0.8}Ru_{0.2}Al$ shows the largest ANE $S_{xy} \sim 23\ \mu$V/K (Figs. 6(a) and 11(b)) and the transverse thermoelectric conductivity $\alpha_{ij} \sim 14$ Am^{-1}K^{-1} at $T \sim 40$ K (Fig. 6(c)) [23]. The crystal structure is noncentrosymmetric hexagonal ZrNiAl-type (space group $P\bar{6}2m$) and U atoms form the distorted Kagome lattice in the *ab* plane (Table 1). The Sommerfeld coefficient for $UCo_{0.8}Ru_{0.2}Al$ is $\gamma \sim 50$ mJ/(mol K^2), indicating moderately heavy charge carriers probably due to electronic correlations. The large σ_{xy} and α_{xy} for $UCo_{0.8}Ru_{0.2}Al$ are reproduced by the first-principles calculations, indicating the large Berry curvature due to topological band structures. Indeed, the first-principles calculations find a large number of Weyl points (148 within $E - E_F \sim \pm 60$ meV), which may contribute to enhancing the Berry curvature and α_{xy}. Although this material is not suitable for applications due to the uranium and low Curie temperature $T_C \sim 56$ K [119], this work provides valuable insight into further enhancement of the ANE.

7. Summary and Perspective

Recent advances in topological condensed matter physics have led to the discovery of large ANEs in a variety of topological magnets, opening the way for their application at room temperature. Since the direction of the ANE-induced electromotive force is controlled by magnetization, even polycrystalline samples can generate strong signals [24, 105, 106], which is beneficial for industrial applications. ANE is better suited for flexible thin-wire circuit architectures, compared to the conventional Seebeck effect. Various ANE-based thermoelectric devices including high-sensitivity thin-film heat flow sensors have been fabricated, and some are fabricated by the mass-producible roll-to-roll sputtering method [34] and ready to be available commercially.

On the other hand, there is still room for improving their functionalities, in particular, for power generation. As discussed in Sec. 6, the magnitude of ANE is still much smaller than the Seebeck effect, resulting in a small figure of merit $Z_{xy}T \sim 0.001$ [18]. In addition to the band engineering relying on the intrinsic AHE, the extrinsic contributions such as magnon-driven ANE (e.g., MnBi [58]) would provide a new route for enhancing ANE. Another important aspect is the zero-field spontaneous ANE in bulk form. As already known in the field of permanent magnets [70], rare-earth magnets with large magnetocrystalline anisotropy would be suitable, though they are costlier. In addition to these functionalities, high Curie temperature, cost-effectiveness, and figure of merit in polycrystalline samples are important factors, while satisfying all the conditions would be rather challenging. Nevertheless, we believe that the innovative work reviewed in this article will inspire future research and uncover novel physical properties and functionalities in magnetic materials to improve the ANE.

8. Acknowledgements

We thank Taishi Chen, Tomoya Higo, Takahiro Tomita, Zili Feng, Agustinus Agung Nugroho, Yangming Wang, Rombang Sihombing, Mingxuan Fu, Ikhlas Muhammad, Daisuke Nishio-Hamane, Rieko Ishii, Shinji Miwa, Yoshichika Otani, Collin Broholm, Peter Armitage for experimental collaboration and Susumu Minami, Yo Pierre Mizuta, Pallab Goswami, Ryotaro Arita, Fumiyuki Ishii, Takashi Koretsune, Michi-To Suzuki, Takuya Nomoto, Nayuta Takemori, Motoaki Hirayama, Motoharu Kitatani, Oleg Tchernyshyov for theoretical support. This work was partially supported by JSTMirai Program (JPMJMI20A1), JST-ASPIRE (JPMJAP2317,25H01250) and JSPSKAKENHI (JP23K03298). The work at the Institute for Quantum Matter, an Energy Frontier Research Center was funded by DOE, Office of Science, Basic Energy Sciences under Award # DE-SC0019331.

References

[1] Bell LE. Cooling, heating, generating power, and recovering waste heat with thermoelectric systems. Science. 2008;321(5895):1457–1461.

[2] Glatz W, Schwyter E, Durrer L, et al. Bi_2Te_3-based flexible micro thermoelectric generator with optimized design. J Microelectromech Syst. 2009 June;18(3):763– 772.

[3] Hu G, Edwards H, Lee M. Silicon integrated circuit thermoelectric generators with a high specific power generation capacity. Nat Electron. 2019;.

[4] Sakuraba Y, Hasegawa K, Mizuguchi M, et al. Anomalous Nernst effect in L10FePt/MnGa thermopiles for new thermoelectric applications. Appl Phys Express. 2013 mar;6(3):033003.

[5] Mizuguchi M, Nakatsuji S. Energy-harvesting materials based on the anomalous Nernst effect. Sci Tech Adv Mater. 2019;20(1):262–275.

[6] Uchida Ki, Zhou W, Sakuraba Y. Transverse thermoelectric generation using magnetic materials. Applied Physics Letters. 2021;118(14).

[7] Nakatsuji S, Arita R. Topological magnets: Functions based on Berry phase and multipoles. Annu Rev of Condens Matter Phys. 2022;13:119–142.

[8] Hasan MZ, Kane CL. Colloquium: Topological insulators. Rev Mod Phys. 2010 Nov;82:3045–3067.

[9] Qi XL, Zhang SC. Topological insulators and superconductors. Rev Mod Phys. 2011 Oct;83:1057–1110.

[10] Ando Y. Topological insulator materials. J Phys Soc Jpn. 2013;82(10):102001.

[11] Armitage N, Mele E, Vishwanath A. Weyl and Dirac semimetals in threedimensional solids. Rev Mod Phys. 2018;90(1):015001.

[12] Wan X, Turner AM, Vishwanath A, et al. Topological semimetal and Fermi-arc surface states in the electronic structure of pyrochlore iridates. Phys Rev B. 2011 May;83:205101.

[13] Burkov AA, Balents L. Weyl semimetal in a topological insulator multilayer. Phys Rev Lett. 2011 Sep;107:127205.

[14] Fang C, Chen Y, Kee HY, et al. Topological nodal line semimetals with and without spin-orbital coupling. Phys Rev B. 2015 Aug;92:081201.

[15] Nakatsuji S, Kiyohara N, Higo T. Large anomalous Hall effect in a non-collinear antiferromagnet at room temperature. Nature. 2015;527(7577):212.

[16] Ikhlas M, Tomita T, Koretsune T, et al. Large anomalous Nernst effect at room temperature in a chiral antiferromagnet. Nat Phys. 2017;13(11):1085–1090.

[17] Li X, Xu L, Ding L, et al. Anomalous Nernst and Righi-Leduc effects in Mn_3Sn: Berry curvature and entropy flow. Phys Rev Lett. 2017 Aug;119:056601.

[18] Sakai A, Mizuta YP, Nugroho AA, et al. Giant anomalous Nernst effect and quantum-critical scaling in a ferromagnetic semimetal. Nat Phys. 2018; 14(11):1119–1124.

[19] Liu E, Sun Y, Kumar N, et al. Giant anomalous Hall effect in a ferromagnetic kagome-lattice semimetal. Nat Phys. 2018 Nov;14(11):1125–1131.

[20] Guin SN, Vir P, Zhang Y, et al. Zero-field Nernst effect in a ferromagnetic kagome-lattice Weyl-semimetal $Co_3Sn_2S_2$. Adv Mater. 2019;31(25):1806622.

[21] Sakai A, Minami S, Koretsune T, et al. Iron-based binary ferromagnets for transverse thermoelectric conversion. Nature. 2020;581(7806):53–57.
[22] Chen T, Tomita T, Minami S, et al. Anomalous transport due to Weyl fermions in the chiral antiferromagnets Mn_3X, X = Sn, Ge. Nat Commun. 2021 Jan; 12(1):572.
[23] Asaba T, Ivanov V, Thomas S, et al. Colossal anomalous Nernst effect in a correlated noncentrosymmetric kagome ferromagnet. Sci Adv. 2021;7(13):eabf1467.
[24] Chen T, Minami S, Sakai A, et al. Large anomalous Nernst effect and nodal plane in an iron-based kagome ferromagnet. Sci adv. 2022;8(2):eabk1480.
[25] Pan Y, Le C, He B, et al. Giant anomalous Nernst signal in the antiferromagnet $YbMnBi_2$. Nat Mater. 2022;21(2):203–209.
[26] Guo X, Li X, Zhu Z, et al. Onsager reciprocal relation between anomalous transverse coefficients of an anisotropic antiferromagnet. Phys Rev Lett. 2023 Dec; 131:246302.
[27] Manna K, Sun Y, Muechler L, et al. Heusler, Weyl and Berry. Nat Rev Mater. 2018;3(8):244–256.
[28] Smejkal L, MacDonald AH, Sinova J, et al. Anomalous Hall antiferromagnets.˘ Nat Rev Mater. 2022 Jun;7(6):482–496.
[29] Narita H, Ikhlas M, Kimata M, et al. Anomalous Nernst effect in a microfabricated thermoelectric element made of chiral antiferromagnet Mn_3Sn. Appl Phys Lett. 2017;111(20).
[30] Zhou W, Sakuraba Y. Heat flux sensing by anomalous Nernst effect in Fe–Al thin films on a flexible substrate. Appl Phys Express. 2020 mar;13(4):043001.
[31] Higo T, Li Y, Kondou K, et al. Omnidirectional control of large electrical output in a topological antiferromagnet. Adv FunctMater. 2021;31(15):2008971.
[32] Uchida Ki, Zhou W, Sakuraba Y. Transverse thermoelectric generation using magnetic materials. Appl Phys Lett. 2021;118(14).
[33] Li X, Zhu Z, Behnia K. A monomaterial Nernst thermopile with hermaphroditic legs. Advanced Materials. 2021;33(20):2100751.
[34] Tanaka H, Higo T, Uesugi R, et al. Roll-to-roll printing of anomalous Nernst thermopile for direct sensing of perpendicular heat flux. Adv Mater. 2023; 35(38):2303416.
[35] Takigawa H, Taguchi T, Takahashi T, et al. Fabrication of thermoelectric ribbonshaped Fe_3Al alloys with large anomalous Nernst effect. 2023 IEEE International Magnetic Conference (INTERMAG). 2023;.
[36] Onsager L. Reciprocal relations in irreversible processes. i. Phys Rev. 1931 Feb; 37:405–426.
[37] Onsager L. Reciprocal relations in irreversible processes. ii. Phys Rev. 1931 Dec; 38:2265–2279.
[38] Callen HB. The application of Onsager's reciprocal relations to thermoelectric, thermomagnetic, and galvanomagnetic effects. Phys Rev. 1948 Jun;73:1349–1358.
[39] Hall EH. On a new action of the magnet on electric currents. Am J Math. 1879; 2(3):287–292.

[40] Hall E. Xviii. on the “rotational coefficient” in nickel and cobalt. The London, Edinburgh, and Dublin Philosophical Magazine and Journal of Science. 1881; 12(74):157–172.
[41] Chien C. The Hall effect and its applications. Springer Science & Business Media; 2013.
[42] Fert A, Reyren N, Cros V. Magnetic skyrmions: advances in physics and potential applications. Nat Rev Mater. 2017 Jun;2(7):17031.
[43] Tokura Y, Kanazawa N. Magnetic skyrmion materials. Chem Rev. 2021 Mar; 121(5):2857–2897.
[44] R¨oßler UK, Bogdanov AN, Pfleiderer C. Spontaneous skyrmion ground states in magnetic metals. Nature. 2006 Aug;442(7104):797–801.
[45] Neubauer A, Pfleiderer C, Binz B, et al. Topological Hall effect in the *a* phase of MnSi. Phys Rev Lett. 2009 May;102:186602.
[46] Yu XZ, Onose Y, Kanazawa N, et al. Real-space observation of a two-dimensional skyrmion crystal. Nature. 2010 Jun;465(7300):901–904.
[47] Nagaosa N, Tokura Y. Topological properties and dynamics of magnetic skyrmions. Nat Nanotechnol. 2013;8:899–911.
[48] Fert A, Cros V, Sampaio J. Skyrmions on the track. Nat Nanotechnol. 2013 Mar; 8(3):152–156.
[49] Shindou R, Nagaosa N. Orbital ferromagnetism and anomalous Hall effect in antiferromagnets on the distorted fcc lattice. Phys Rev Lett. 2001 Aug;87:116801.
[50] Martin I, Batista CD. Itinerant electron-driven chiral magnetic ordering and spontaneous quantum Hall effect in triangular lattice models. Phys Rev Lett. 2008 Oct;101:156402.
[51] Machida Y, Nakatsuji S, Onoda S, et al. Time-reversal symmetry breaking and spontaneous Hall effect without magnetic dipole order. Nature. 2010 Jan; 463(7278):210–213.
[52] Smejkal L, Sinova J, Jungwirth T. Emerging research landscape of altermag-ˇ netism. Phys Rev X. 2022 Dec;12:040501.
[53] Jungwirth T, Sinova J, Fernandes RM, et al. Symmetry, microscopy and spectroscopy signatures of altermagnetism. arXiv preprint arXiv:250622860. 2025;
.
[54] Ray MK, Fu M, Chen Y, et al. Zero-field Hall effect emerging from a non-Fermi liquid in a collinear antiferromagnet $V_{1/3}NbS_2$. Nat Commun. 2025;16(1):3532.
[55] Takagi R, Hirakida R, Settai Y, et al. Spontaneous Hall effect induced by collinear antiferromagnetic order at room temperature. Nat Mater. 2025; 24(1):63–68.
[56] Modak R, Sakuraba Y, Hirai T, et al. Sm-Co-based amorphous alloy films for zero-field operation of transverse thermoelectric generation. Science and Technology of Advanced Materials. 2022;23(1):767–782.
[57] Berry MV. Quantal phase factors accompanying adiabatic changes. Proceedings of the Royal Society of London A Mathematical and Physical Sciences. 1984; 392(1802):45–57.

[58] He B, S¸ahin C, Boona SR, et al. Large magnon-induced anomalous Nernst conductivity in single-crystal MnBi. Joule. 2021;5(11):3057–3067.
[59] Nagaosa N, Sinova J, Onoda S, et al. Anomalous Hall effect. Rev Mod Phys. 2010 May;82:1539–1592.
[60] Xiao D, Chang MC, Niu Q. Berry phase effects on electronic properties. Rev Mod Phys. 2010 Jul;82:1959–2007.
[61] Thouless DJ, Kohmoto M, Nightingale MP, et al. Quantized Hall conductance in a two-dimensional periodic potential. Phys Rev Lett. 1982 Aug;49:405–408.
[62] Chen H, Niu Q, MacDonald AH. Anomalous Hall effect arising from noncollinear antiferromagnetism. Phys Rev Lett. 2014 Jan;112:017205.
[63] Suzuki MT, Koretsune T, Ochi M, et al. Cluster multipole theory for anomalous Hall effect in antiferromagnets. Phys Rev B. 2017 Mar;95:094406.
[64] Xiao D, Yao Y, Fang Z, et al. Berry-phase effect in anomalous thermoelectric transport. Phys Rev Lett. 2006 Jul;97:026603.
[65] Sharma G, Goswami P, Tewari S. Nernst and magnetothermal conductivity in a lattice model of Weyl fermions. Phys Rev B. 2016 Jan;93:035116.
[66] Minami S, Ishii F, Hirayama M, et al. Enhancement of the transverse thermoelectric conductivity originating from stationary points in nodal lines. Phys Rev
B. 2020 Nov;102:205128.
[67] Yang KY, Lu YM, Ran Y. Quantum Hall effects in a Weyl semimetal: Possible application in pyrochlore iridates. Phys Rev B. 2011 Aug;84:075129.
[68] Nielsen H, Ninomiya M. Absence of neutrinos on a lattice: (I). proof by homotopy theory. Nuc Phys B. 1981;185(1):20–40.
[69] Onoda S, Sugimoto N, Nagaosa N. Quantum transport theory of anomalous electric, thermoelectric, and thermal Hall effects in ferromagnets. Phys Rev B. 2008 Apr;77:165103.
[70] Coey J. Perspective and prospects for rare earth permanent magnets. Engineering. 2020;6(2):119–131.
[71] Kr´en E, Paitz J, Zimmer G, et al. Study of the magnetic phase transformation in the Mn_3Sn phase. Physica B+C. 1975;80(1):226–230.
[72] Tomiyoshi S. Polarized neutron diffraction study of the spin structure of Mn_3Sn. J Phy Soc Jpn. 1982;51(3):803–810.
[73] Brown PJ, Nunez V, Tasset F, et al. J Phys Condens Matter. 1990 Nov;
2(47):9409.
[74] Yamada N, Sakai H, Mori HY, et al. Magnetic properties of ε-Mn_3Ge. Physica B+C. 1988;149(1):311–315.
[75] Sukhanov AS, Singh S, Caron L, et al. Gradual pressure-induced change in the magnetic structure of the noncollinear antiferromagnet Mn_3Ge. Phys Rev B. 2018 Jun;97:214402.
[76] Kiyohara N, Tomita T, Nakatsuji S. Giant anomalous Hall effect in the chiral antiferromagnet Mn_3Ge. Phys Rev Appl. 2016 Jun;5:064009.
[77] Nayak AK, Fischer JE, Sun Y, et al. Large anomalous hall effect driven by a nonvanishing Berry curvature in the noncolinear antiferromagnet Mn_3Ge. Sci Adv. 2016;2(4):e1501870.

[78] Higo T, Man H, Gopman DB, et al. Large magneto-optical Kerr effect and imaging of magnetic octupole domains in an antiferromagnetic metal. Nat Photon. 2018 Feb;12(2):73–78.
[79] Matsuda T, Kanda N, Higo T, et al. Room-temperature terahertz anomalous Hall effect in Weyl antiferromagnet Mn_3Sn thin films. Nat Commun. 2020 Feb; 11(1):909.
[80] Kimata M, Chen H, Kondou K, et al. Magnetic and magnetic inverse spin Hall effects in a non-collinear antiferromagnet. Nature. 2019 Jan;565(7741):627–630.
[81] Tsai H, Higo T, Kondou K, et al. Electrical manipulation of a topological antiferromagnetic state. Nature. 2020 Apr;580(7805):608–613.
[82] Tsai H, Higo T, Kondou K, et al. Large Hall signal due to electrical switching of an antiferromagnetic Weyl semimetal state. Small Science. 2021;1(5):2000025.
[83] Higo T, Kondou K, Nomoto T, et al. Perpendicular full switching of chiral antiferromagnetic order by current. Nature. 2022 Jul;607(7919):474–479.
[84] Chen X, Higo T, Tanaka K, et al. Octupole-driven magnetoresistance in an antiferromagnetic tunnel junction. Nature. 2023 Jan;613(7944):490–495.
[85] Hayami S, Yanagi Y, Kusunose H. Bottom-up design of spin-split and reshaped electronic band structures in antiferromagnets without spin-orbit coupling: Procedure on the basis of augmented multipoles. Phys Rev B. 2020 Oct;102:144441.
[86] Kuroda K, Tomita T, Suzuki MT, et al. Evidence for magnetic Weyl fermions in a correlated metal. Nature Materials. 2017 Nov;16(11):1090–1095.
[87] Jungwirth T, Marti X, Wadley P, et al. Antiferromagnetic spintronics. Nature Nanotechnology. 2016 Mar;11(3):231–241.
[88] Han J, Cheng R, Liu L, et al. Coherent antiferromagnetic spintronics. Nature Materials. 2023 Jun;22(6):684–695.
[89] Rimmler BH, Pal B, Parkin SSP. Non-collinear antiferromagnetic spintronics. Nat Rev Mater. 2025 Feb;10(2):109–127.
[90] Guin SN, Manna K, Noky J, et al. Anomalous Nernst effect beyond the magnetization scaling relation in the ferromagnetic Heusler compound Co_2MnGa. NPG Asia Mater. 2019 Apr;11(1):16.
[91] Xu L, Li X, Ding L, et al. Anomalous transverse response of Co_2MnGa and universality of the room-temperature $\alpha_{ij}^A/\sigma_{ij}^A$ ratio across topological magnets. Phys Rev B. 2020 May;101:180404.
[92] Uesugi R, Higo T, Nakatsuji S. Giant anomalous Nernst effect in polycrystalline thin films of the Weyl ferromagnet Co_2MnGa. Appl Phys Lett. 2023;123(25).
[93] Webster P. Magnetic and chemical order in Heusler alloys containing cobalt and manganese. J Phys Chem Solids. 1971;32(6):1221–1231.
[94] Belopolski I, Manna K, Sanchez DS, et al. Discovery of topological Weyl fermion lines and drumhead surface states in a room temperature magnet. Science. 2019; 365(6459):1278–1281.
[95] Sumida K, Sakuraba Y, Masuda K, et al. Spin-polarized Weyl cones and giant anomalous Nernst effect in ferromagnetic Heusler films. Commun Mater. 2020 Nov;1(1):89.

[96] Kono T, Kakoki M, Yoshikawa T, et al. Three-dimensional bulk Fermi surfaces and Weyl crossings of Co_2MnGa thin films underneath a protection layer. Phys Rev B. 2021 Nov;104:195112.
[97] Belopolski I, Chang G, Cochran TA, et al. Observation of a linked-loop quantum state in a topological magnet. Nature. 2022 Apr;604(7907):647–652.
[98] Leiva L, Granville S, Zhang Y, et al. Giant spin Hall angle in the Heusler alloy Weyl ferromagnet Co_2MnGa. Phys Rev B. 2021 Jan;103:L041114.
[99] Isshiki H, Zhu Z, Mizuno H, et al. Determination of spin Hall angle in the Weyl ferromagnet Co_2MnGa by taking into account the thermoelectric contributions. Phys Rev Mater. 2022 Aug;6:084411.
[100] Harman TC, Honig JM. Theory of galvano-thermomagnetic energy conversion devices. I. Generators. J Appl Phys. 1962;33(11):3178–3188.
[101] Sakuraba Y, Hyodo K, Sakuma A, et al. Giant anomalous nernst effect in the $Co_2MnAl_{1-x}Si_x$ heusler alloy induced by fermi level tuning and atomic ordering. Phys Rev B. 2020 Apr;101:134407.
[102] Kawamiya N, Adachi K, Nakamura Y. Magnetic properties and M¨ossabauer investigations of Fe-Ga alloys. J Phys Soc Jpn. 1972;33(5):1318–1327.
[103] Shinohara T. The effect of atomic ordering on the magnetic properties of Fe-Al alloys. J Phys Soc Jpn. 1964;19(1):51–58.
[104] Watzman SJ, Duine RA, Tserkovnyak Y, et al. Magnon-drag thermopower and Nernst coefficient in Fe, Co, and Ni. Phys Rev B. 2016;94(14):144407.
[105] Feng Z, Minami S, Akamatsu S, et al. Giant and robust anomalous Nernst effect in a polycrystalline topological ferromagnet at room temperature. Adv Funct Mater. 2022;32(49):2206519.
[106] Wang Y, Sakai A, Minami S, et al. Robust giant anomalous Nernst effect in polycrystalline nodal web ferromagnets. Appl Phys Lett. 2024 08;125(8):081901.
[107] Nakayama H, Masuda K, Wang J, et al. Mechanism of strong enhancement of anomalous Nernst effect in Fe by Ga substitution. Phys Rev Mater. 2019; 3(11):114412.
[108] Wei Y, Zhang W, Lv B, et al. Ultralow magnetic damping of a common metallic ferromagnetic film. Sci Adv. 2021;7(4):eabc5053.
[109] Sakamoto S, Higo T, Tamaru S, et al. Low gilbert damping in epitaxial thin films of the nodal-line semimetal $D0_3$ Fe_3Ga. Phys Rev B. 2021 Apr;103:165122.
[110] Wang A, Zaliznyak I, Ren W, et al. Magnetotransport study of Dirac fermions in $YbMnBi_2$ antiferromagnet. Phys Rev B. 2016 Oct;94:165161.
[111] Borisenko S, Evtushinsky D, Gibson Q, et al. Time-reversal symmetry breaking type-II Weyl state in $YbMnBi_2$. Nat Commun. 2019 Jul;10(1):3424.
[112] Soh JR, Jacobsen H, Ouladdiaf B, et al. Magnetic structure and excitations of the topological semimetal $YbMnBi_2$. Phys Rev B. 2019 Oct;100:144431.
[113] Mielke A. Ferromagnetism in the Hubbard model on line graphs and further considerations. J Phys A: Math Gen. 1991 jul;24(14):3311.
[114] Tasaki H. Ferromagnetism in the Hubbard models with degenerate singleelectron ground states. Phys Rev Lett. 1992 Sep;69:1608–1611.

[115] Sales BC, Saparov B, McGuire MA, et al. Ferromagnetism of Fe_3Sn and alloys. Scic Rep. 2014 Nov;4(1):7024.
[116] Fujiwara K, Kato Y, Abe H, et al. Berry curvature contributions of kagomelattice fragments in amorphous Fe–Sn thin films. Nat Commun. 2023 Jun; 14(1):3399.
[117] Kurosawa S, Higo T, Saito S, et al. Large spontaneous magneto-thermoelectric effect in epitaxial thin films of the topological kagome ferromagnet Fe_3Sn. Phys Rev Mater. 2024 May;8:054206.
[118] Liu DF, Liang AJ, Liu EK, et al. Magnetic Weyl semimetal phase in a kagom´e crystal. Science. 2019;365(6459):1282–1285.
[119] Posp´ıˇsil J, Opletal P, Valiˇska M, et al. Properties and collapse of the ferromagnetism in $UCo_{1-x}Ru_xAl$ studied in single crystals. J Phys Soc Jpn. 2016; 85(3):034710.
[120] Miyasato T, Abe N, Fujii T, et al. Crossover behavior of the anomalous Hall effect and anomalous Nernst effect in itinerant ferromagnets. Phys Rev Lett. 2007 Aug;99:086602.
[121] Manyala N, Sidis Y, DiTusa JF, et al. Large anomalous Hall effect in a siliconbased magnetic semiconductor. Nat Mater. 2004 Apr;3(4):255–262.

Figures

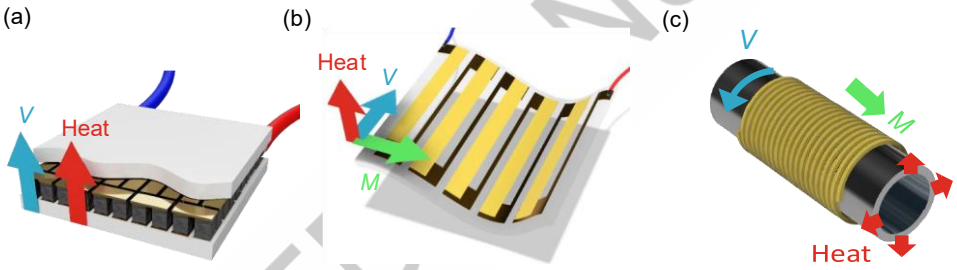

Figure 1. Schematic figures of thermoelectric devices based on the longitudinal (a) and transverse (b, c) thermoelectric effects (Adapted from [21]). In the Seebeck-effect-based (Peltier) device, a large number of pand n-type semiconductor pillars are necessary to enhance the output voltage. In contrast, ANE-based devices can achieve increased output voltage in a thin-film form, which is suitable for covering large areas and curved heat sources.

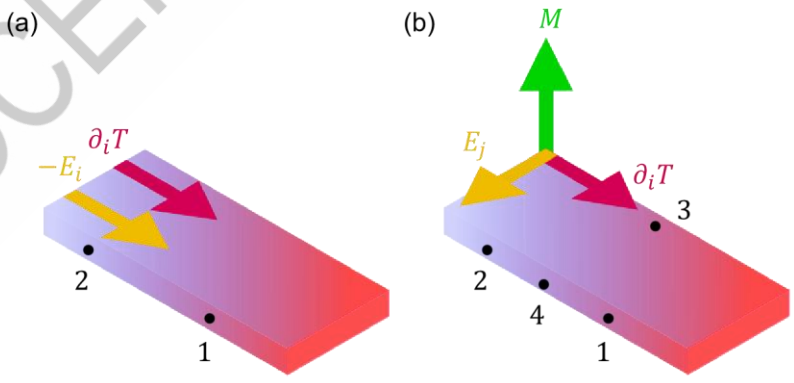

$$S_{ii} = \frac{E_i}{-\partial_i T} = \frac{(V_1 - V_2)/\ell}{(T_1 - T_2)/\ell} = \frac{\Delta V_{1-2}}{\Delta T_{1-2}} \qquad S_{ji} = \frac{E_j}{-\partial_i T} = \frac{(V_3 - V_4)/\ell_V}{(T_1 - T_2)/\ell_T} = \frac{\ell_T}{\ell_V}\frac{\Delta V_{3-4}}{\Delta T_{1-2}}$$

Figure 2. Schematic figures illustrating the Seebeck effect (a) and ANE (b). For the Seebeck coefficient S_{ii}, the sample length ℓ appears in both numerator and denominator and cancels out. As a result, S_{ii} is determined solely by the ratio of voltage to temperature difference $\Delta V_{1-2}/\Delta T_{1-2}$. In contrast, the sample dimension remains for the anomalous Nernst coefficient S_{ij} as $S_{ij} = (\ell_T/\ell_V)(\Delta V_{3-4}/\Delta T_{1-2})$, where $\ell_T = \ell_{1-2}$ and $\ell_V = \ell_{3-4}$ respectively represent length between thermometers along the heat current direction and length between transverse voltage terminals. This means that the ANE voltage ΔV_{3-4} increases by reducing ℓ_T and increasing ℓ_V, as realized in thin-film ANE-based thermoelectric modules (see Fig. 1(b) and (c)).

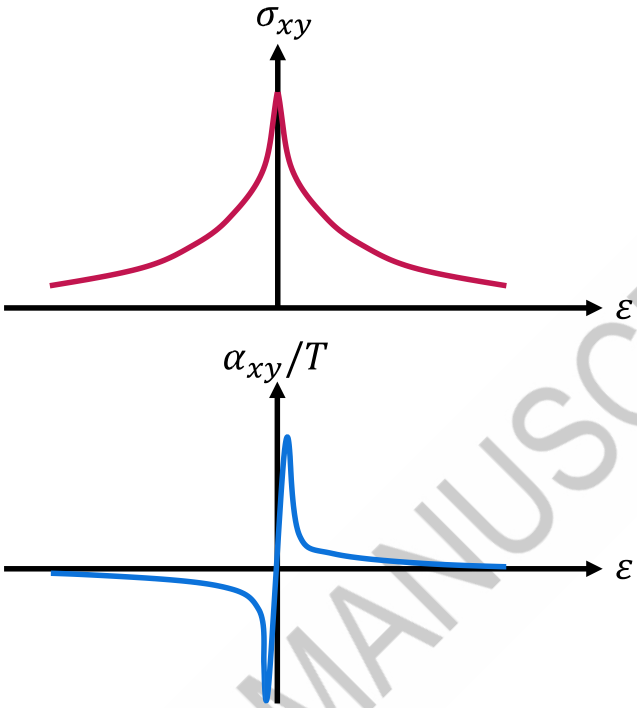

Figure 3. Schematic figures for the energy dependence of σ_{xy} (top) and α_{xy} (bottom) at low temperatures, where the Mott relation (Eq. (22)) holds [65]. Here, we assume topological band structure (e.g., Weyl points and nodal lines) inducing a large Berry curvature Ω_z at Fermi energy $\varepsilon \sim 0$.

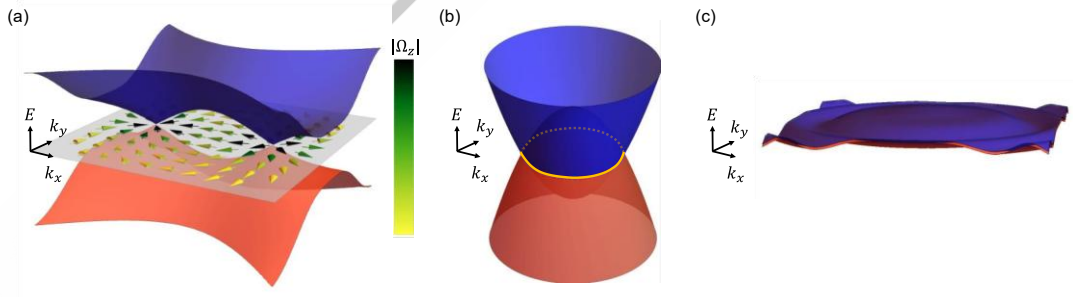

Figure 4. Schematic figures for topological band structures; (a) nodal points (Weyl points), (b) a nodal line and (c) a nodal plane. The arrows in (a) show the directions and magnitudes of the Berry curvature.

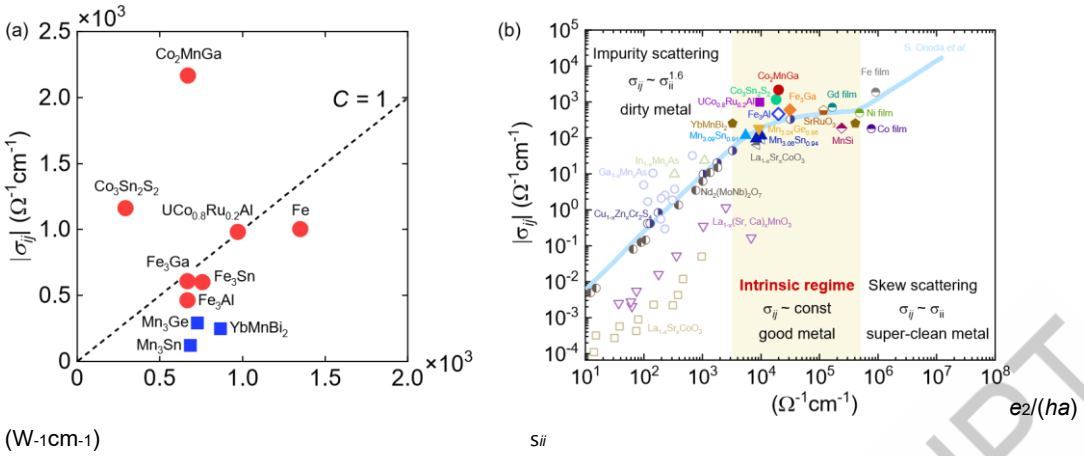

Figure 5. (a) The magnitude of the anomalous Hall conductivity $|\sigma_{ij}|$ compared to $e^2/(ha)$, where a is the lattice constant along the applied field direction; $a = b = c = 5.77$ ˚A for Co_2MnGa, 5.80 ˚A for Fe_3Ga, 5.79 ˚A for Fe_3Al, 2.89 ˚A for Fe, $a = b = 5.66$ ˚A for Mn_3Sn $a = b = 5.33$ ˚A for Mn_3Ge, $a = b = 4.47$ ˚A for $YbMnBi_2$, $c = 13.18$ ˚A for $Co_3Sn_2S_2$, $c = 3.97$ ˚A for $UCo_{0.8}Ru_{0.2}Al$. For polycrystalline Fe_3Sn, we used the averaged lattice constant $(a + b + c)/3 \sim 5.10$ ˚A. (b) The scaling relation between $|\sigma_{ij}|$ and the longitudinal conductivity σ_{ii}. Here, data taken at the lowest temperature ($T \sim 2$ K) are used except for Mn_3Sn ($T \sim 100$ K). The references include Refs. [15, 16, 22] for Mn_3Sn and Mn_3Ge, Ref. [18] for Co_2MnGa, Ref. [21] for Fe_3Ga and Fe_3Al, Ref. [26] for $YbMnBi_2$, Ref. [24] for Fe_3Sn, Refs. [19, 20] for $Co_3Sn_2S_2$, Ref. [23] for $UCo_{0.8}Ru_{0.2}Al$, Ref. [120] for Fe, Co, Ni and Gd thin films, Ref. [121] for MnSi, Ref. [69] for perovskite oxides ($SrRuO_3$, $La_{1-x}Sr_xCoO_3$, $La_{1-x}(Sr,Ca)_xMnO_3$), spinels ($Cu_{1-x}Zn_xCr_2Se_4$), pyrochlore ($Nd_2(MoNb)_2O_7$) and magnetic semiconductor ($Ga_{1-x}Mn_xAs$, $In_{1-x}Mn_xAs$).

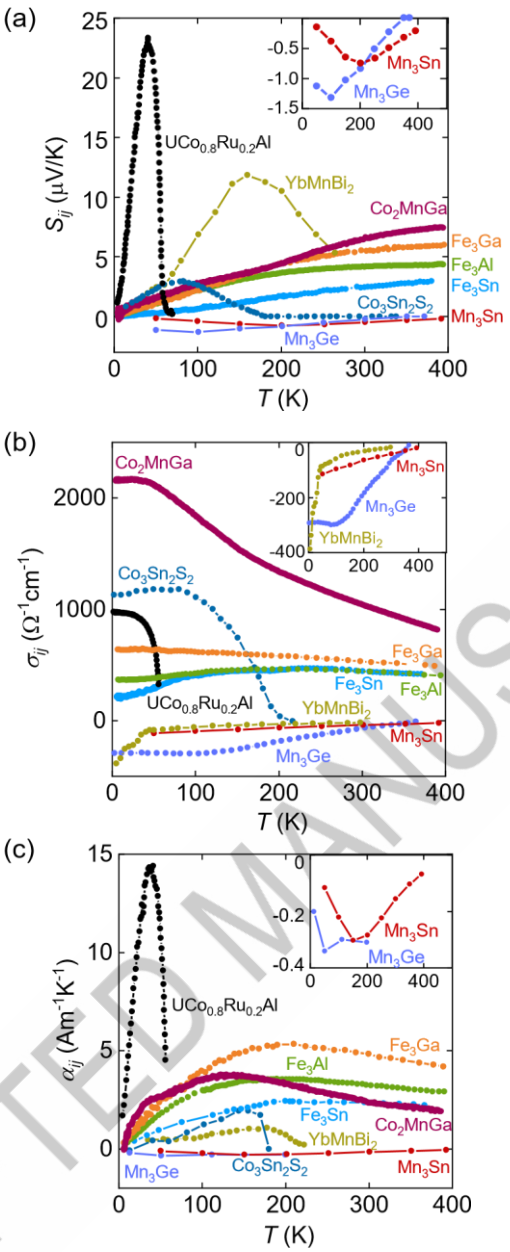

Figure 6. Temperature dependence of the anomalous Nernst coefficient S_{ij} (a), anomalous Hall conductivity σ_{ij} (b) and transverse thermoelectric conductivity α_{ij} (c) for various topological magnets. The measurement conditions, including the directions of electric current (**I**) and heat current (**Q**), are as follows: Mn_3Sn ($Mn_{3.06}Sn_{0.94}$, $ij = zx$, **B** ∥ [01$^-$10],**I**,**Q** ∥ [2$^-$1$^-$10]) [16], Mn_3Ge ($Mn_{3.03}Ge_{0.97}$, $ij = zx$, **B** ∥ [01$^-$10],**I**,**Q** ∥ [2$^-$1$^-$10]) [22], Co_2MnGa ($ij = xy$,**B** ∥ [100],**I**,**Q** ∥ [001]) [18], Fe_3X (X = Ga, Al) ($ij = xy$,**B** ∥ [100],**I**,**Q** ∥ [001]) [21], polycrystalline Fe_3Sn [24], $Co_3Sn_2S_2$ (**B** ∥ [0001], **I**,**Q** ∥ *ab* plane) [19, 20], $UCo_{0.8}Ru_{0.2}Al$ (**B** ∥ **c**, **I**,**Q** ∥ **a**) [23] and $YbMnBi_2$ (−S_{zy},**B** ∥ **x**,**I**,**Q** ∥ **z**)[26]. Insets show zoomed-in region where the y axis is negative.

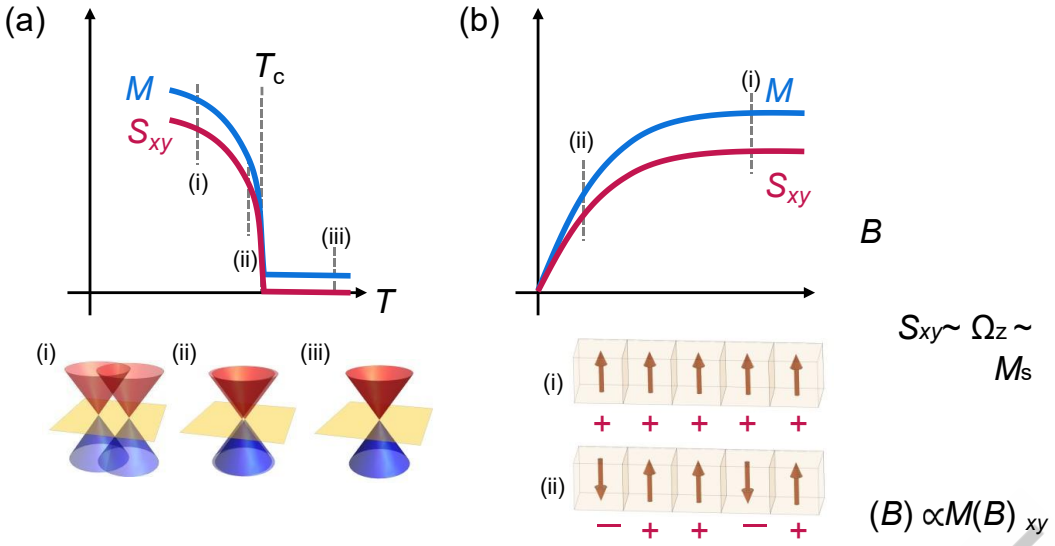

Figure 7. (a) Schematic figures for the T dependences of M and S_{ij} near the Curie temperature T_C (top), and Weyl (or Dirac) points for (i)-(iii). (b) Schematic figures for the B dependences of M and S_{xy} (top), magnetic domains (boxes & red vectors) and their contributions to S_{xy} (signs below boxes). The total M and S_{xy} are obtained by summing over each domain contribution (red vectors and signs, respectively). At high field (e.g., state at (i)), all the magnetic moments are parallel to the applied external field, and thus total S_{xy} reflects the Berry curvature Ω_z, leading to the violation of the empirical scaling relation between the *magnitude* of S_{xy} and saturation magnetization M_s. On the other hand, the *shape* of the B sweep curves are similar to each other; $S_{xy}(B) \propto M(B)$. This is because both the total $S_{xy}(B)$ and $M(B)$ are determined by integrating all the magnetic-domain contributions at low fields (e.g., the state at (ii)). Here, we assume the Ising anisotropy and B applied to the easy axis.

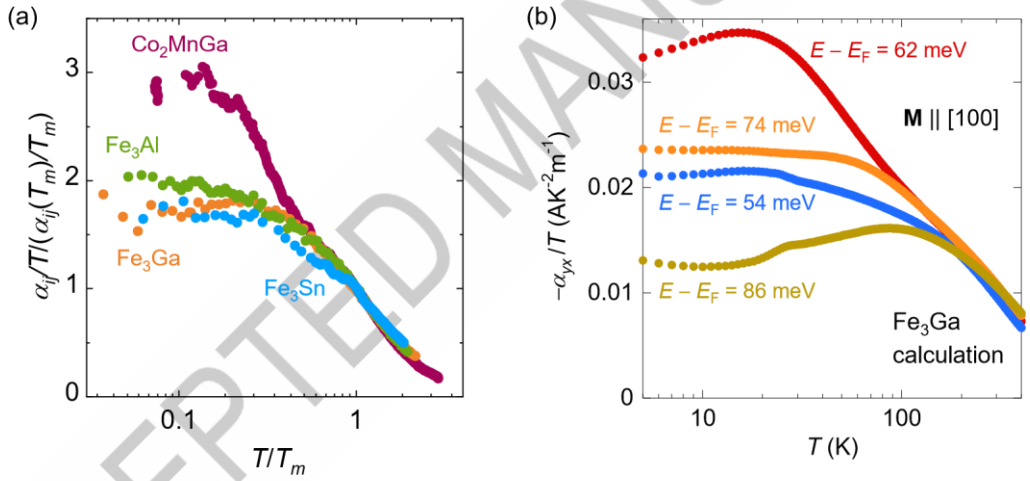

Figure 8. (a) The scaling relation of the transverse thermoelectric coefficient, $\alpha_{ij}/T/(\alpha_{ij}(T_m)/T_m)$ vs T/T_m, for Co_2MnGa [18], Fe_3X (X = Ga, Al) [21] and Fe_3Sn [24]. Here, T_m is the temperature where α_{ij} shows maximum. (b) T dependence of α_{xy}/T at various energy $E - E_F$ obtained from the first-principles calculation for Fe_3Ga. As the energy associated with the topological flat band approaches the Fermi energy, α_{xy} shows $-\ln T$ divergence down to much lower temperatures.

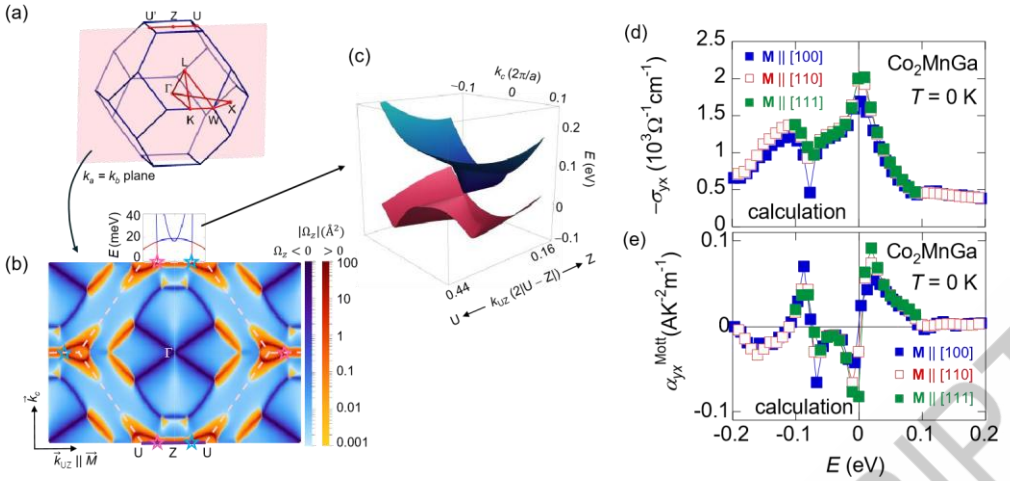

Figure 9. Topological band structure and large transverse responses obtained from the first-principles calculations for Co_2MnGa (Adapted from [18]). (a) First Brillouin zone with $k_a = k_b$ plane highlighted (pink). (b) Berry curvature on $k_a = k_b$ plane. (c) Tilted Weyl cone near the Z-U line. (d, e) Calculated anomalous Hall conductivity $-\sigma_{yx}$ (d) and transverse thermoelectric conductivity α_{yx} (e). Here α_{yx} is obtained from the Mott relation (Eq. 22).

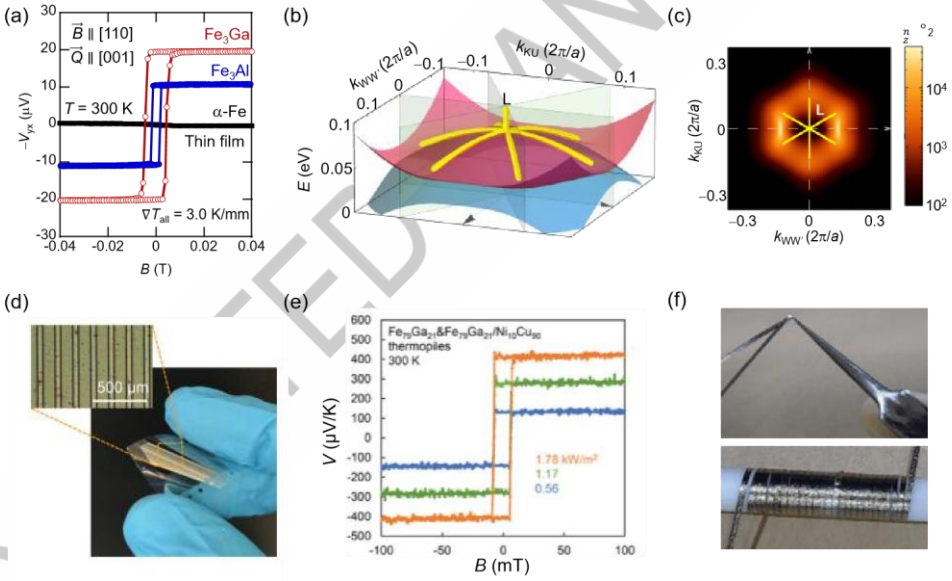

Figure 10. (a) Anomalous Nernst voltages for Fe_3Ga and Fe_3Al epitaxial thin films compared to that for α-Fe. Heat current was applied perpendicular to the film **Q** ∥ [001] and with in-plane magnetic field, **B** ∥ [001]. (b), (c) Topological band structure (nodal web) (b) and Berry curvature (c) near the L point obtained from the first-principles calculations for Fe_3X. ((a)-(c) Adapted from [21]) (d) Flexible Fe_3Ga-based heat flux sensor fabricated on PET (polyethylene terephthalate) substrate. (e) B dependence of the ANE voltage for the Fe_3Ga-based flexible heat flux sensor. Here, in-plane Seebeck effect is compensated by using $Ni_{10}Cu_{90}$ as electrodes since $S_{ii,Co2MnGa} \sim -S_{ii,Ni10Cu90}$. ((d), (e) Adapted from [34]). (d) The ribbon-shaped Fe_3Al (Adapted from [35]).

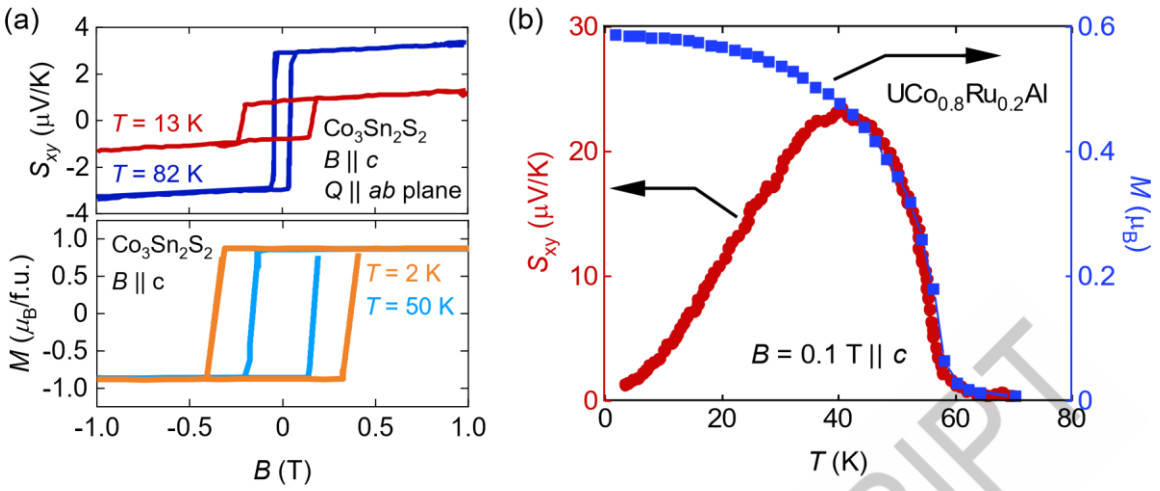

Figure 11. (a) B dependence of S_{xy} (top) and M (bottom) for $Co_3Sn_2S_2$. The data are taken from Ref. [20]. The difference in coercivity between S_{xy} and M can be attributed to the difference in T and sample shape. (b) T dependence of S_{xy} (left axis) and M (right axis) for $UCo_{0.8}Ru_{0.2}Al$. The data are taken from Ref. [23].

Table 1. Crystal structure and spin texture, type of magnetic order (FM or AFM), magnetic ordering temperature (T_C or T_N), bandstructure topology, S_{xy} at room temperature and related references for various topological magnets showing the large ANE.

Material	Crystal structure an spin texture	FM or AFM	T_C or T_N (K)	Band structure topology	S_{xy} at room T (μV/K)	Ref.
Mn_3X (X = Sn, Ge)	Hexagonal Ni_3Sn-type ($D0_{19}$) 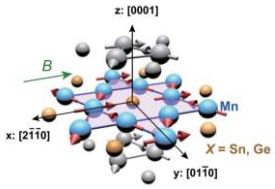 Adapted from [22]	AFM	430 (X = Sn), 372 (X = Ge)	Weyl points	~ −0.5	ANE [16, 17, 22] AHE [15] Device [31] Review [27, 22, 28, 7]
Co_2MnGa, $Co_2MnAl_{1-x}Si_x$	Cubic full Heusler ($L2_1$) 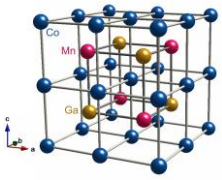	FM	694	Weyl points	~ 8	ANE & AHE [18, 90, 91, 101, 92], Device [32], Review [7]
Fe_3X (X=Ga, Al)	BCC derivative structure ($D0_3$) 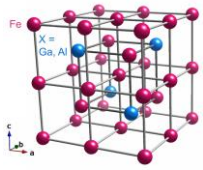	FM	720 (X = Al), 600 (X = Ga)	Nodal lines	~ 4 (X = Al) ~ 6 (X = Ga)	ANE [21, 107, 105, 106], AHE, Device [30, 34, 35], Review [7]
$YbMnBi_2$	tetragonal 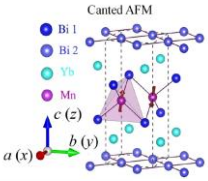 Adapted from [26]	AFM	~290	Weyl points	0 (~ 10 μV/K at T ~ 200 K)	AHE & ANE [25, 26]
Fe_3Sn	hexagonal Ni_3Sn-type ($D0_{19}$) 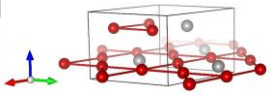 Adapted from [24]	FM	760	Nodal plane	~ 3	AHE & ANE [24, 116, 117]
$Co_3Sn_2S_2$	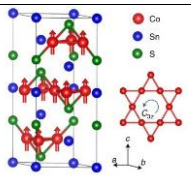 rhombohedral Adapted from [19]	FM	177	Weyl points	0 (~ 3 μV/K at T ~ 75 K)	ANE [20], AHE [19]

$UCo_{0.8}Ru_{0.2}Al$	hexagonal ZrNiAl-type 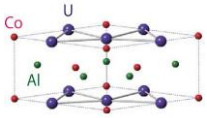 Adapted from [23]	FM 27	56	Weyl points	0 (~ 23 μV/K at $T \sim 40$ K)	AHE [119] ANE [23]

Akito Sakai is a Lecturer at Department of Physics, University of Tokyo. He received his Ph.D. from University of Tokyo in 2011. From 2014 to 2016, he worked at University of Augsburg in Germany as JSPS Postdoctoral Fellowship for Research Abroad. In 2016, he served as a Project Research Associate at Institute for Solid State Physics (ISSP) and became Research Associate in 2017. In 2020, he became a lecturer at Department of Physics, University of Tokyo. His current research explores novel quantum phenomena induced by strong electron correlations and topological band structures.

Satoru Nakatsuji is a Professor at Department of Physics, Project Professor at ISSP, the Director of Trans-Scale Quantum Science Institute, University of Tokyo. He also serves as Research Professor in the Department of Physics and Astronomy at Johns

Hopkins University, Project Manager for Mirai-Project Large Scale, JST, Japan and a Fellow in CIFAR, Canada. He received his Ph.D in Physics from the Kyoto University in 2001 and then worked as a postdoc at National High Magnetic Field Laboratory in Florida till 2003. After he served as a Lecturer of the Department of Physics at Kyoto University from 2003 to 2006, he moved to University of Tokyo as an Associate Professor of the ISSP and later became a Full Professor in 2016. In 2019, he joined the faculty of Department of Physics of University of Tokyo as a Full Professor. His research is in the areas of quantum materials and quantum electronics. The emphasis is on studies of relativistic particles and novel quantum phenomena in matter, room-temperature quantum transport and spintronics of topological magnetic materials, and quantum phase transitions in strongly correlated electron systems.

We review recently developed transverse thermoelectric generation technology using topological magnets and cover its novel mechanism and applications.